nature nanotechnology

ARTICLES

https://doi.org/10.1038/s41565-021-00951-y

Check for updates

Synergizing metal–support interactions and spatial confinement boosts dynamics of atomic nickel for hydrogenations

Jian Gu[1,7], Minzhen Jian[1,7], Li Huang[2,7], Zhihu Sun[2], Aowen Li[3], Yang Pan[2], Jiuzhong Yang[2], Wu Wen[2], Wu Zhou[3,4], Yue Lin[1], Hui-Juan Wang[5], Xinyu Liu[1], Leilei Wang[1], Xianxian Shi[1], Xiaohui Huang[1], Lina Cao[1], Si Chen[1], Xusheng Zheng[2], Haibin Pan[2], Junfa Zhu[2], Shiqiang Wei[2]✉, Wei-Xue Li[1,6]✉ and Junling Lu[1,6]✉

Atomically dispersed metal catalysts maximize atom efficiency and display unique catalytic properties compared with regular metal nanoparticles. However, achieving high reactivity while preserving high stability at appreciable loadings remains challenging. Here we solve the challenge by synergizing metal–support interactions and spatial confinement, which enables the fabrication of highly loaded atomic nickel (3.1 wt%) along with dense atomic copper grippers (8.1 wt%) on a graphitic carbon nitride support. For the semi-hydrogenation of acetylene in excess ethylene, the fabricated catalyst shows extraordinary catalytic performance in terms of activity, selectivity and stability—far superior to supported atomic nickel alone in the absence of a synergizing effect. Comprehensive characterization and theoretical calculations reveal that the active nickel site confined in two stable hydroxylated copper grippers dynamically changes by breaking the interfacial nickel–support bonds on reactant adsorption and making these bonds on product desorption. Such a dynamic effect confers high catalytic performance, providing an avenue to rationally design efficient, stable and highly loaded, yet atomically dispersed, catalysts.

Supported atomically dispersed catalysts (SADCs) have recently drawn great attention in numerous reactions for their maximized atom efficiency[1,2]. Exclusive site homogeneity, distinct energetics and spatial site confinement make SADCs very attractive in high selectivity and alleviated coke formation in the conversion of hydrocarbons[3–5], sharply distinct from the low selectivity and heavy coke formation on metal nanoparticle (NP) catalysts[6]. However, owing to drastically increased surface free energies, the stability of atomically dispersed metal species under reaction conditions, especially at high metal loadings, has been the key issue to substantially limit the overall performance, restraining their practical applications[7].

Realization of a highly loaded and stable SADC for hydrogenation reactions is particularly challenging, because atomically dispersed metal species often show higher mobility in reducing environments[8]. For instance, in the semi-hydrogenation of acetylene in excess ethylene, a crucial industrial process operated at a scale of billions of tons per annum to purify alkene streams[9,10], severe metal aggregations occurred even for low-loaded SADCs, which sequentially generated heavy coke formation—an even worse scenario to further accelerate catalyst deactivation to a shorter lifetime[11]. Increasing metal–support interactions (MSIs)[12,13] or confining active metal species in restrained spaces (for example, micropores)[14,15] are two widely adopted methodologies to achieve higher stability. However, excessively strong MSIs might over-stabilize the active sites and cause low activity[13,16]; confinement of metal species in micropores might also limit mass transfers[14,17]. Consequently, a seesaw relation between stability and activity has been often observed, obscuring efforts for catalytic performance optimizations[18–20].

In this work, we report that the challenge can be solved by synergizing MSIs and spatial confinement to break the activity–stability seesaw of SADCs at high metal loadings. Specifically, strong Ni–N/C interaction and spatial confinement by dense atomic Cu grippers (8.1 wt%) on a graphitic carbon nitride (g-C_3N_4) support are synergized to endow great structural flexibility of highly loaded (3.1 wt%) atomic Ni with reversible bond breakings and makings on reactant adsorption and product desorption, respectively. Such a dynamic effect not only facilitates acetylene adsorption for high activity but also ensures high thermal/chemical stability and unprecedented inhibition of coke formation.

Results

Synthesis and catalytic performance. As it contains periodic triangular cavities with six coordinately unsaturated pyridinic nitrogen (N_{py}) atoms, g-C_3N_4 provides a perfect platform for anchoring active and dense metal species[21,22]. Screening of metals among groups VIII and IB by density functional theory (DFT) calculations revealed that Ni and Cu atoms exhibit strong binding to g-C_3N_4 underneath

[1]Hefei National Laboratory for Physical Sciences at the Microscale, Department of Chemical Physics, Key Laboratory of Surface and Interface Chemistry and Energy Catalysis of Anhui Higher Education Institutes, CAS Center for Excellence in Nanoscience, University of Science and Technology of China, Hefei, China. [2]National Synchrotron Radiation Laboratory, University of Science and Technology of China, Hefei, China. [3]School of Physical Sciences and CAS Key Laboratory of Vacuum Physics, University of Chinese Academy of Sciences, Beijing, China. [4]CAS Center for Excellence in Topological Quantum Computation, University of Chinese Academy of Sciences, Beijing, China. [5]Experimental Center of Engineering and Materials Science, University of Science and Technology of China, Hefei, China. [6]Dalian National Laboratory for Clean Energy, Dalian Institute of Chemical Physics, Chinese Academy of Sciences, Dalian, China. [7]These authors contributed equally: Jian Gu, Minzhen Jian, Li Huang. ✉e-mail: sqwei@ustc.edu.cn; wxli70@ustc.edu.cn; junling@ustc.edu.cn

along with low formation energy (Supplementary Table 1); therefore, they are the most promising candidates for highly loaded and stable metals on g-C_3N_4 with atomic dispersion.

Inspired by these results, atomic layer deposition (ALD), a gas-phase technique relying on sequential self-limiting molecular-level surface reactions[23,24], was employed to deposit Cu and Ni with near-atomic precision[25,26]. Atomic Cu grippers were first fabricated on g-C_3N_4 by Cu ALD (denoted as Cu_1/g-C_3N_4), as confirmed by X-ray absorption spectroscopy and aberration-corrected high-angle annular dark-field scanning transmission electron microscopy (HAADF-STEM), where the saturated loading was ~11.2 wt% (Supplementary Figs. 1a and 2–5 and Supplementary Table 2). Ni_yCu_1/g-C_3N_4 catalysts (y is the atomic ratio of Ni to Cu) were synthesized by depositing Ni on subsaturated Cu_1/g-C_3N_4 using NiO_x ALD, as shown in the schematic and morphology in Supplementary Figs. 6 and 7, respectively. Therein, the Ni loadings decreased with an increase in Cu loadings (Supplementary Fig. 1b), which implies that at Cu subsaturation coverages, the open N_{py} sites along with neighbouring Cu atoms provide anchoring sites for guest atoms, analogous to pincer ligands in organometallic chemistry[27]. For comparison, Ni_1/g-C_3N_4 SADCs were also fabricated by NiO_x ALD (Supplementary Figs. 8–12 and Supplementary Table 3). HAADF-STEM measurements showed that Cu_1/g-C_3N_4, Ni_1/g-C_3N_4 and Ni_1Cu_x/g-C_3N_4 were thermally stable at 350 °C under H_2 (Supplementary Figs. 13–15), in line with the above theoretical prediction.

Next, three samples, namely, Cu_1/g-C_3N_4 (8.1 wt%), Ni_1/g-C_3N_4 (3.1 wt%), and Ni_1Cu_2/g-C_3N_4 with similar loadings of Cu (8.1 wt%) and Ni (3.1 wt%), were evaluated in the selective hydrogenation of acetylene in excess ethylene. We found that compared with Cu_1/g-C_3N_4 and Ni_1/g-C_3N_4, Ni_1Cu_2/g-C_3N_4 showed much higher activity by achieving 100% conversion at ~170 °C (Fig. 1a). Importantly, the ethylene selectivity was as high as 90% even at full acetylene conversion (Fig. 1b), which is desirable for practical applications[28]. The corresponding activity was 7.01 h^{-1} at 160 °C, about 11 and 58 times higher than that of Ni_1/g-C_3N_4 and Cu_1/g-C_3N_4, respectively (Fig. 1c). Kinetics measurements further confirmed the activity trend (Supplementary Fig. 16).

Remarkably, in addition to high thermal stability, Ni_1Cu_2/g-C_3N_4 showed unprecedented chemical stability under hydrogenation conditions, without any visible decline in either activity or selectivity for at least 350 h at 160 °C, and the used sample remained structurally intact (Fig. 1d and Supplementary Figs. 17–19). In sharp contrast, Ni_1/g-C_3N_4 showed a slight activity increase approximately in the first six hours, and then rapidly deactivated with an activity loss of ~50% in about 50 h. X-ray diffraction (XRD) and HAADF-STEM measurements also revealed severe agglomeration of Ni atoms into Ni particles (Supplementary Figs. 19 and 20).

State-of-the-art in situ synchrotron vacuum ultraviolet photoionization mass spectrometry (SVUV-PIMS) revealed that besides C_2 products, considerable gaseous C_3–C_8 species were produced from Ni_1/g-C_3N_4 (Fig. 1e and Supplementary Fig. 21), indicating the facile formation of green oils. In contrast, no higher hydrocarbons formed on Ni_1Cu_2/g-C_3N_4, except a trace amount of C_4H_8. Temperature-programmed desorption (TPD) SVUV-PIMS measurements of the two samples after 2 h of reaction further showed negligible accumulation of C_{4+} species on Ni_1Cu_2/g-C_3N_4 (Fig. 1f and Supplementary Figs. 22 and 23), unambiguously confirming the complete inhibition of the formation of green oils on Ni_1Cu_2/g-C_3N_4.

Coke formation was further quantitatively monitored by in situ thermogravimetric analysis (TGA) under hydrogenation conditions. After 12 h, the weight gain of Ni_1Cu_2/g-C_3N_4 was negligible, close to the thermal noise. However, Ni_1/g-C_3N_4 showed a considerable weight increase by 7.6% (Fig. 1g), in line with the above SVUV-PIMS measurements. Meanwhile, the XRD data revealed the formation of graphitic coke on Ni_1/g-C_3N_4 (Supplementary Fig. 19), but not for Ni_1Cu_2/g-C_3N_4. Clearly, the capability of coke inhibition and long durability achieved on Ni_1Cu_2/g-C_3N_4 is unprecedented, far superior to the benchmark catalysts reported in the literature (Table 1 and Supplementary Tables 4–6). Besides the above, Ni_1Cu_2/g-C_3N_4 also exhibited extraordinary performance in the semi-hydrogenation of 1,3-butadiene in excess propene (Supplementary Fig. 24), rendering this material promising for wide applications.

Structural characterization. Statistical analysis of atomic-resolution STEM images of these samples found that there were mainly three structural motifs, namely, single atoms, linear trimers and triangular trimers (Fig. 2a and Supplementary Figs. 5, 7, and 12). For Cu_1/g-C_3N_4, single atoms were the most populated (68%), followed by linear trimers (20%) and triangular trimers (12%) (Supplementary Fig. 25). Subsequent Ni deposition forms Ni_1Cu_2/g-C_3N_4, and linear trimers increased dramatically (71%) at the expense of single atoms (18%), while triangular trimers remained at ~11% (Fig. 2b). This suggests that most of the predeposited single Cu atoms were likely bridged by Ni atoms to form new linear trimers (Supplementary Fig. 6). Atomic-resolution electron energy-loss spectroscopy (EELS) elemental mapping of one linear trimer at a relatively low beam current to minimize electron-beam perturbations (Supplementary Fig. 26) further provided strong evidence of the linear Cu–Ni–Cu trimer structure, by identifying a Ni atom in the middle and two Cu atoms on the adjacent sides (Fig. 2c,d). The overall lengths of the linear trimers were 5.66 ± 0.20 Å comprising two unequal atom–atom distances of 2.61 ± 0.14 and 3.04 ± 0.13 Å on average (Supplementary Fig. 7).

To confirm direct Cu–Ni interactions, in situ diffuse reflectance infrared Fourier transform spectroscopy (DRIFTS) of CO chemisorption measurements were carried out. As shown in Fig. 2e and Supplementary Fig. 27, Cu_1/g-C_3N_4 showed one dominant peak at 2,103 cm^{-1} and a weak shoulder at 2,123 cm^{-1}, assigned to linear CO on isolated Cu^+ ions and trimers, respectively[29]. CO chemisorption on Ni_1/g-C_3N_4 was negligible. Deposition of Ni atoms on Cu_1/g-C_3N_4 gradually diminished the intensity of the CO peak, strongly verifying the direct Cu–Ni interactions. On $Ni_1(3.1\%)Cu_1(8.1\%)$/g-C_3N_4 (the optimized Ni_1Cu_2/g-C_3N_4 sample), when considering the Cu:Ni mole ratio of 2.4:1.0, the trivial CO peak strongly confirms that one Ni is approximately coordinated with two Cu atoms but without forming Ni particles/clusters, in line with the formation of Ni_1Cu_2 linear trimers (Supplementary Fig. 28). Analysis of the CO peak areas before and after Ni deposition reveals that Ni_1Cu_2 linear trimers might be about 87% in Ni_1Cu_2/g-C_3N_4, agreeing well with the STEM statistics (Fig. 2b). A control experiment of depositing Ni on a Cu_1/C_3N_4 sample at low Cu loading revealed that a high density of Cu_1 atoms is essential to form Ni_1Cu_2 linear trimers (Supplementary Fig. 29).

C_2H_2 and C_2H_4 TPD were also applied to probe direct Ni–Cu interactions. We found that the main C_2H_2 desorption peak of Ni_1Cu_2/g-C_3N_4 was located at 107 °C, sharply different from that of Cu_1/g-C_3N_4 (146 °C) and Ni_1/g-C_3N_4 (82 °C), further supporting the formation of Ni_1Cu_2 linear trimers (Supplementary Fig. 30). Meanwhile, the tailing C_2H_2 desorption peak of Ni_1Cu_2/g-C_3N_4 (146 °C) coincided with that of Cu_1/g-C_3N_4, suggesting the coexistence of isolated Cu atoms. Quantitative analysis of the TPD spectrum reveals that the percentage of Ni_1Cu_2 linear trimers is about 74% (Fig. 2b), close to the STEM statistics (71%). Analysis of C_2H_4 TPD showed the same result. Considering the negligible activity of Cu_1/g-C_3N_4, Ni_1/g-C_3N_4 and $Ni_1(1\%)Cu_1(0.5\%)$/g-C_3N_4 below 170 °C (Fig. 1a and Supplementary Fig. 29), the exceptional performance of Ni_1Cu_2/g-C_3N_4 should come solely from the prevailing linear trimers.

In situ X-ray photoemission spectroscopy (XPS) showed that the Cu2$p^{3/2}$ binding energy was invariant at 933.2 eV, irrespective of

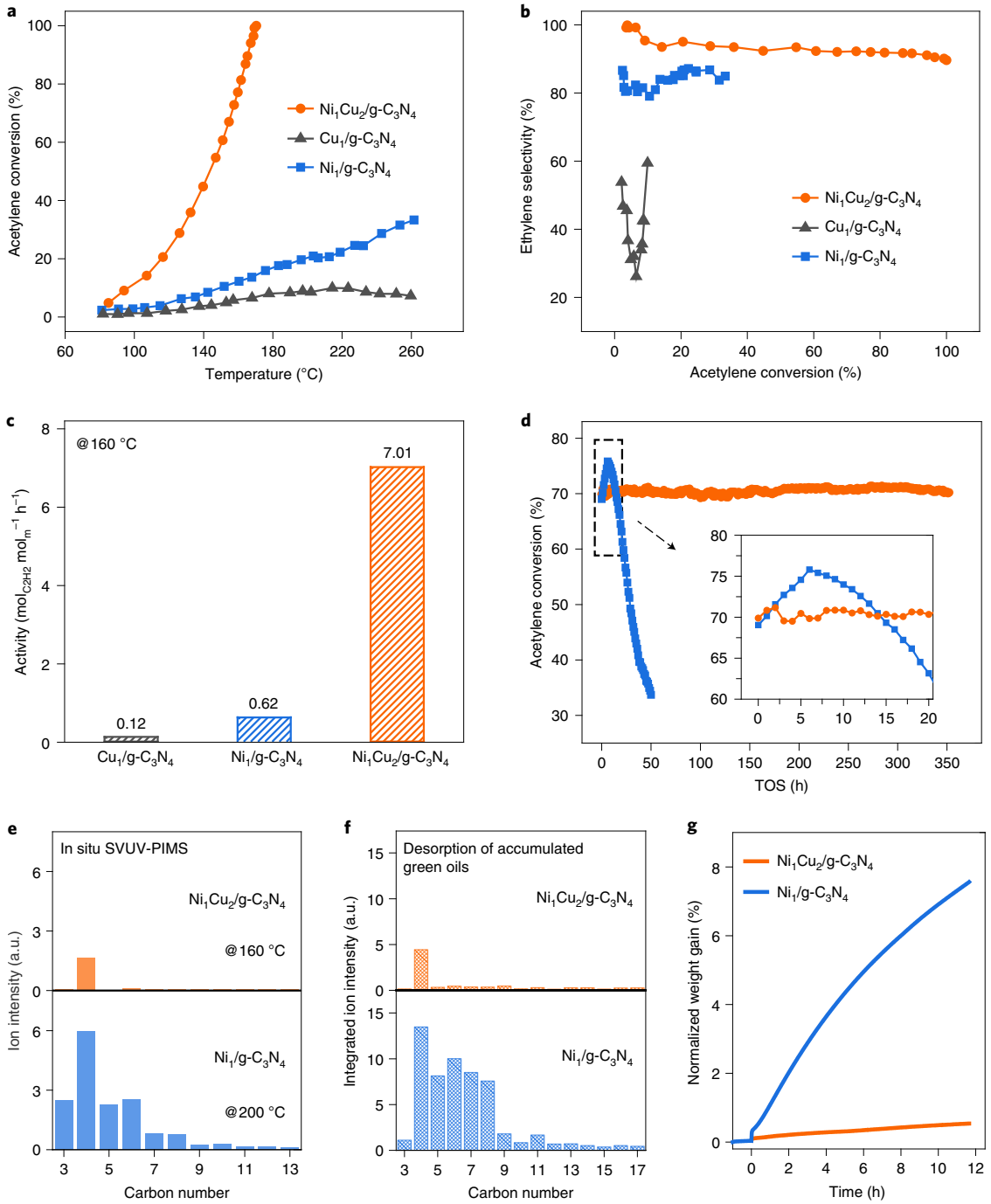

Fig. 1 | Catalytic performance of Ni–Cu pincer complex catalyst. a,**b**, Acetylene conversion as a function of temperature (**a**) and ethylene selectivity as a function of acetylene conversion (**b**) over Ni_1Cu_2/g-C_3N_4, Cu_1/g-C_3N_4 and Ni_1/g-C_3N_4 catalysts. **c**, Activity of these three samples at 160 °C. m, metal (Cu or Ni). **d**, Time-on-stream (TOS) stability with the same initial conversion of 70% at different temperatures. The inset shows the expanded conversion changes in the first 20 h, with the same *x*- and *y*-axis labels as the main figure. Reaction conditions: 0.5% C_2H_2, 5% H_2 and 25% C_2H_4 balanced with Ar; the space velocity is 12,000 ml g^{-1} h^{-1} and the pressure is 0.1 MPa. **e**, Distributions of volatile C_n ($n = 3, 4, 5\ldots$) gas-phase products at the reactor outlet during reactions on Ni_1Cu_2/g-C_3N_4 and Ni_1/g-C_3N_4 catalysts from in situ SVUV-PIMS measurements in the stable region. **f**, Distributions of the desorption of accumulated C_n ($n = 3, 4, 5\ldots$) green oils on these two samples in 2 h of reaction. **g**, In situ TGA measurements of coke deposition on Ni_1Cu_2/g-C_3N_4 and Ni_1/g-C_3N_4 catalysts under reaction conditions at 160 and 200 °C, respectively.

the treatments—an indication of the +1 oxidation state[27,30] (Fig. 2f and Supplementary Fig. 31), which is in line with the DRIFTS CO chemisorption data (Fig. 2e). The Ni2$p^{3/2}$ binding energy located at 855.8 eV, close to that of $Ni(OH)_2$ (ref. [31]). Along with this, considerable hydroxyl-type oxygen, with O1*s* at 531.4 eV, was found. Quantitative XPS analysis showed that the stoichiometric ratio between O and Ni was about 2:1. Taken together, these results suggest that the active linear trimers are $Ni_1(OH)_2Cu_2$ complexes formed under the reaction conditions.

To reveal the structure of the $Ni_1(OH)_2Cu_2$ complexes in Ni_1Cu_2/g-C_3N_4, in situ X-ray absorption spectroscopy measurements were further conducted (Supplementary Fig. 15). At the Ni K edge,

Table 1 | Catalytic performances of benchmark catalysts reported in the literature in the semi-hydrogenation of acetylene

Catalysts	Morphology	Total transition metal loadings (wt%)	Ethylene selectivity (%)[a]	TOS (h)	Average deactivation rate[b] (% h^{-1})	Coke formation	Notes
$Ni_1Cu_2/g\text{-}C_3N_4$	Trimeric ions	11.2	90	350	0	N.D.[f]	This work
$Ni_1/g\text{-}C_3N_4$	Single ions	3.1	85	50	0.71	Yes	This work
Na-Ni@CHA	Single ions	3.5	97	50	0.28	Yes	Ref. [37]
Ni-SAs/N-C	Single ions	1.5	90	18	0.61	N.A.[e]	Ref. [38]
Cu_1/ND@G	Single ions	0.2	98	60	0	N.A.[e]	Ref. [9]
$0.5Cu/Al_2O_3$	Single ions	0.5	91	40	0	Yes	Ref. [39]
Pd_1/ND@G	Single ions	0.11	90	30	0	N.D.[f]	Ref. [40]
ISA-Pd/MPNC	Single ions	0.043	82	20	0.05	N.A.[e]	Ref. [41]
$AgPd_{0.01}/SiO_2$	SAAs[c]	4.91	80	24	0.25	N.A.[e]	Ref. [42]
$AuPd_{0.01}/SiO_2$	SAAs[c]	4.92	70	24	0.71	Yes	Ref. [43]
NiGa	IMC[d]	10.0	75	24	0.04	Yes	Ref. [44]
$Ni_3Ga/MgAl_2O_4$	IMC[d]	2.0	77	24	0.16	Yes	Ref. [45]
$Al_{13}Fe_4$	IMC[d]	N.A.[e]	82	20	0.55	Yes	Ref. [46]
PdZn	IMC[d]	N.A.[e]	91	20	0.20	Yes	Ref. [47]
Nano-$GaPd_2$	IMC[d]	N.A.[e]	72	20	0.25	Yes	Ref. [48]
Pre-NiCu/MMO	Bimetallic NPs	19.7	70	16	1.56	Yes	Ref. [49]
$NiIn/SiO_2$	Bimetallic NPs	8.0	35	10	6.91	Yes	Ref. [50]

[a]Ethylene selectivity was determined at near 100% acetylene conversion. [b]The average deactivation rate was determined by the decrease in acetylene conversion divided by TOS. [c]Single-atom alloys. [d]Intermetallic compound. [e]Not available. [f]Not detectable.

the extended X-ray absorption fine-structure (EXAFS) curve of $Ni_1Cu_2/g\text{-}C_3N_4$ after 350 °C hydrogen reduction ($Ni_1Cu_2/g\text{-}C_3N_4$-R) was nearly identical to that under the hydrogenation condition ($Ni_1Cu_2/g\text{-}C_3N_4$-H) (Fig. 2g). The main peak at 1.41 Å is assigned to Ni–O/N/C scattering, and the weak peak at 2.21 Å is attributed to Ni–O/N/C and Ni–Cu coordination according to wavelet transform (Supplementary Fig. 32). Quantitative EXAFS fitting revealed that the coordination numbers (CNs) for the nearest Ni–O/N/C and Ni–Cu were 3.3 and 0.8 with bond distances of 1.96 and 2.90 Å, respectively (Supplementary Fig. 33 and Supplementary Table 7). Similarly, at the Cu K edge, $Ni_1Cu_2/g\text{-}C_3N_4$-R and $Ni_1Cu_2/g\text{-}C_3N_4$-H appeared at the same structure. The main peak at 1.47 Å was attributed to Cu–O/NC coordination with a CN of 1.7, and the weak peak at 2.33 Å was assigned to Cu–Cu/Ni coordination with a CN of 0.5 (Fig. 2h, Supplementary Fig. 34 and Supplementary Table 8).

Spectroscopic insight into the hydrogenation process. In situ DRIFTS measurements were carried out to investigate the catalytic roles of hydroxyl groups. We found that as $Ni_1/g\text{-}C_3N_4$ was exposed to acetylene at 160 °C, two negative peaks appeared at 3,568 and 3,430 cm^{-1}, assigned to Ni–OH groups (Fig. 3a and Supplementary Figs. 35 and 36)[32]. The consumption of hydroxyls is attributed to their reaction with acetylene and Ni aggregations to Ni/NiO_x particles (Supplementary Figs. 20 and 37). Meanwhile, IR bands in the ranges of 3,200–3,300, 2,900–3,200 and 2,800–2,900 cm^{-1} gradually increased in intensity with time, assigned to the vibrations of gas-phase acetylene, ν(C–H) of chemisorbed acetylene and $\nu(CH_3)$ of ethylidene/ethylidyne, respectively (where ν represents stretching vibrations)[33]. Switching the gas to hydrogen, the peaks of all C–H stretching declined, indicating the formation of ethylene and ethane. However, the Ni–OH groups were not recovered. Repeating the above experiments for another acetylene–hydrogen cycle showed a similar result.

In sharp contrast to $Ni_1/g\text{-}C_3N_4$, the consumption and regeneration of Ni–OH groups at 3,581 and 3,440 cm^{-1} on $Ni_1Cu_2/g\text{-}C_3N_4$ was totally reversible during sequential acetylene and hydrogen exposures, implying that the Ni–OH group directly participates in the hydrogenation reaction (Fig. 3b). Interestingly, there was a lack of any features in the range of 2,800–2,900 cm^{-1}, suggesting that much less ethane was formed on $Ni_1Cu_2/g\text{-}C_3N_4$. Meanwhile, exposing $Ni_1Cu_2/g\text{-}C_3N_4$ to ethylene did not cause any consumption of OH groups (Supplementary Fig. 38). These findings unambiguously support the high ethylene selectivity of $Ni_1Cu_2/g\text{-}C_3N_4$ (Fig. 1b). Finally, in situ DRIFTS of C_2H_2 hydrogenation on the

Fig. 2 | Structural characterization. a, Representative HAADF-STEM image of $Ni_1Cu_2/g\text{-}C_3N_4$ with atomic resolution, where representative isolated atoms, triangular trimers and linear trimers are highlighted by dashed yellow circles, red triangles and green rectangles, respectively. **b**, Statistics of single atoms, linear trimers and triangular trimers in $Ni_1Cu_2/g\text{-}C_3N_4$ using four different approaches, namely, HAADF-STEM, DRIFTS CO chemisorption, C_2H_2 TPD and C_2H_4 TPD. **c**, Intensity profile and atomic-resolution EELS elemental mapping of an individual linear trimer shown in the inset. **d**, Atomic-resolution EELS spectra collected at the corresponding positions in **c**. **e**, In situ DRIFT spectra of CO chemisorption on $Ni_1(x\%)Cu_1(8.1\%)/g\text{-}C_3N_4$ catalysts with different Ni loadings (x%). The spectrum of CO chemisorption on $Ni_1(3.1\%)/g\text{-}C_3N_4$ is also shown for comparison. **f**, In situ Cu2*p*, Ni2*p* and O1s XPS spectra of $Ni_1Cu_2/g\text{-}C_3N_4$ after treatments of 350 °C reduction and acetylene hydrogenation reaction at 160 °C. **g**,**h**, In situ k^3-weighted Fourier transform (FT) spectra of $Ni_1Cu_2/g\text{-}C_3N_4$ after reduction and under reaction conditions at the Ni (**g**) and Cu (**h**) K edges; references of Ni foil, NiO, NiPc, Cu foil, Cu_2O and CuPc are also presented for comparison. R in **g** and **h** represents the distance between the absorbing atom and neighbouring scattering atoms, without correcting for scattering phase shift. $\chi(k)$ denotes the amplitude of the EXAFS oscillations as a function of photoelectron wavenumber k. a.u., arbitrary units.

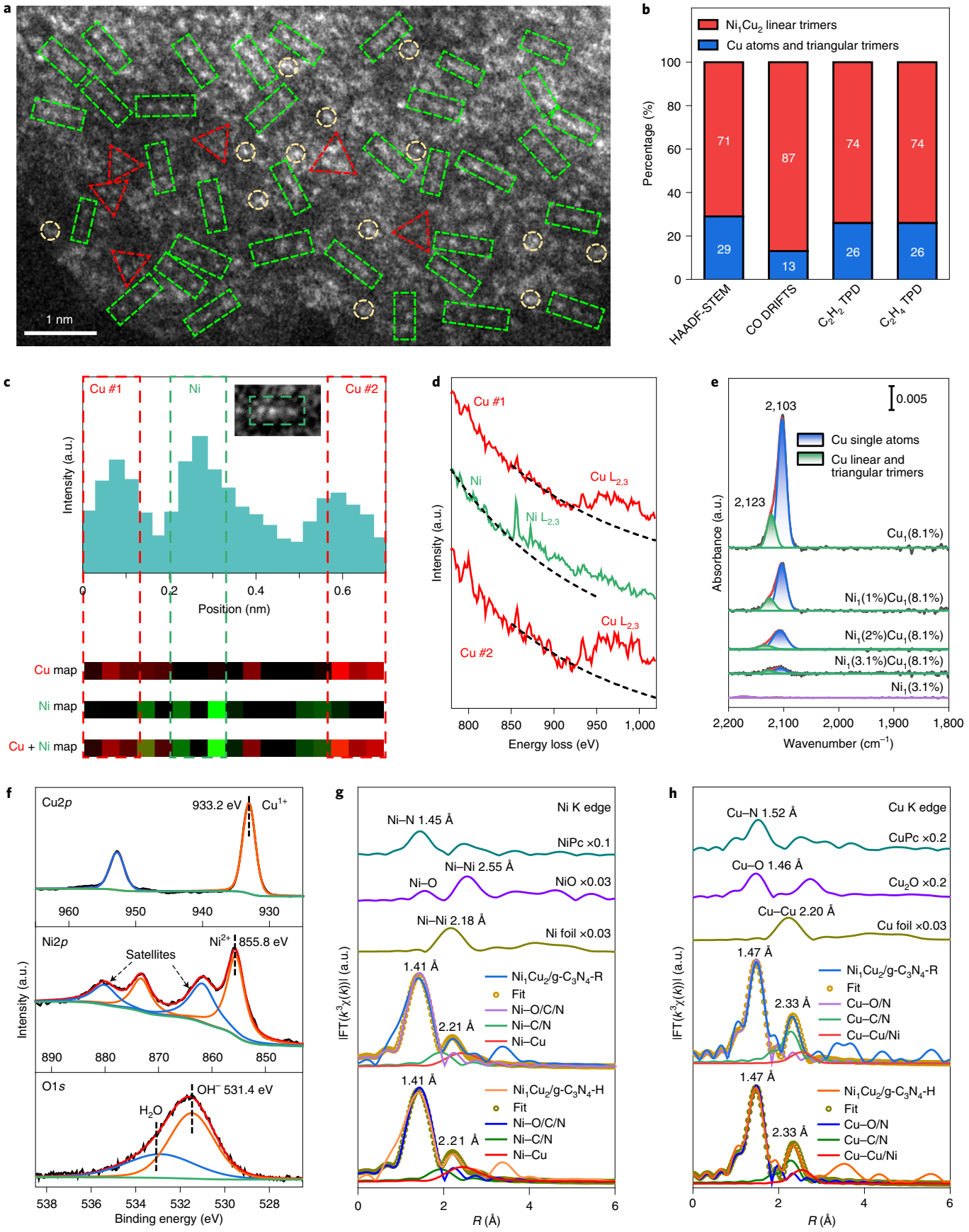
a
1 nm
b
Ni1Cu2 linear trimers
Cu atoms and triangular trimers
Percentage (%)
71
29
87
13
74
26
74
26
HAADF-STEM
CO DRIFTS
C2H2 TPD
C2H4 TPD
c
Cu #1
Ni
Cu #2
Intensity (a.u.)
Position (nm)
Cu map
Ni map
Cu + Ni map
d
Cu #1
Ni
Cu L2,3
Ni L2,3
Cu #2
Intensity (a.u.)
Energy loss (eV)
e
2,103
0.005
Cu single atoms
Cu linear and triangular trimers
2,123
Cu1(8.1%)
Ni1(1%)Cu1(8.1%)
Ni1(2%)Cu1(8.1%)
Ni1(3.1%)Cu1(8.1%)
Ni1(3.1%)
Absorbance (a.u.)
Wavenumber (cm−1)
f
Cu2p
933.2 eV
Cu1+
Ni2p
Satellites
Ni2+ 855.8 eV
O1s
OH− 531.4 eV
H2O
Intensity (a.u.)
Binding energy (eV)
g
Ni K edge
Ni–N 1.45 Å
NiPc ×0.1
Ni–Ni 2.55 Å
Ni–O
NiO ×0.03
Ni–Ni 2.18 Å
Ni foil ×0.03
1.41 Å
2.21 Å
Ni1Cu2/g-C3N4-R
Fit
Ni–O/C/N
Ni–C/N
Ni–Cu
Ni1Cu2/g-C3N4-H
IFT(k3χ(k))| (a.u.)
R (Å)
h
Cu K edge
Cu–N 1.52 Å
CuPc ×0.2
Cu–O 1.46 Å
Cu2O ×0.2
Cu–Cu 2.20 Å
Cu foil ×0.03
1.47 Å
2.33 Å
Cu–O/N
Cu–C/N
Cu–Cu/Ni

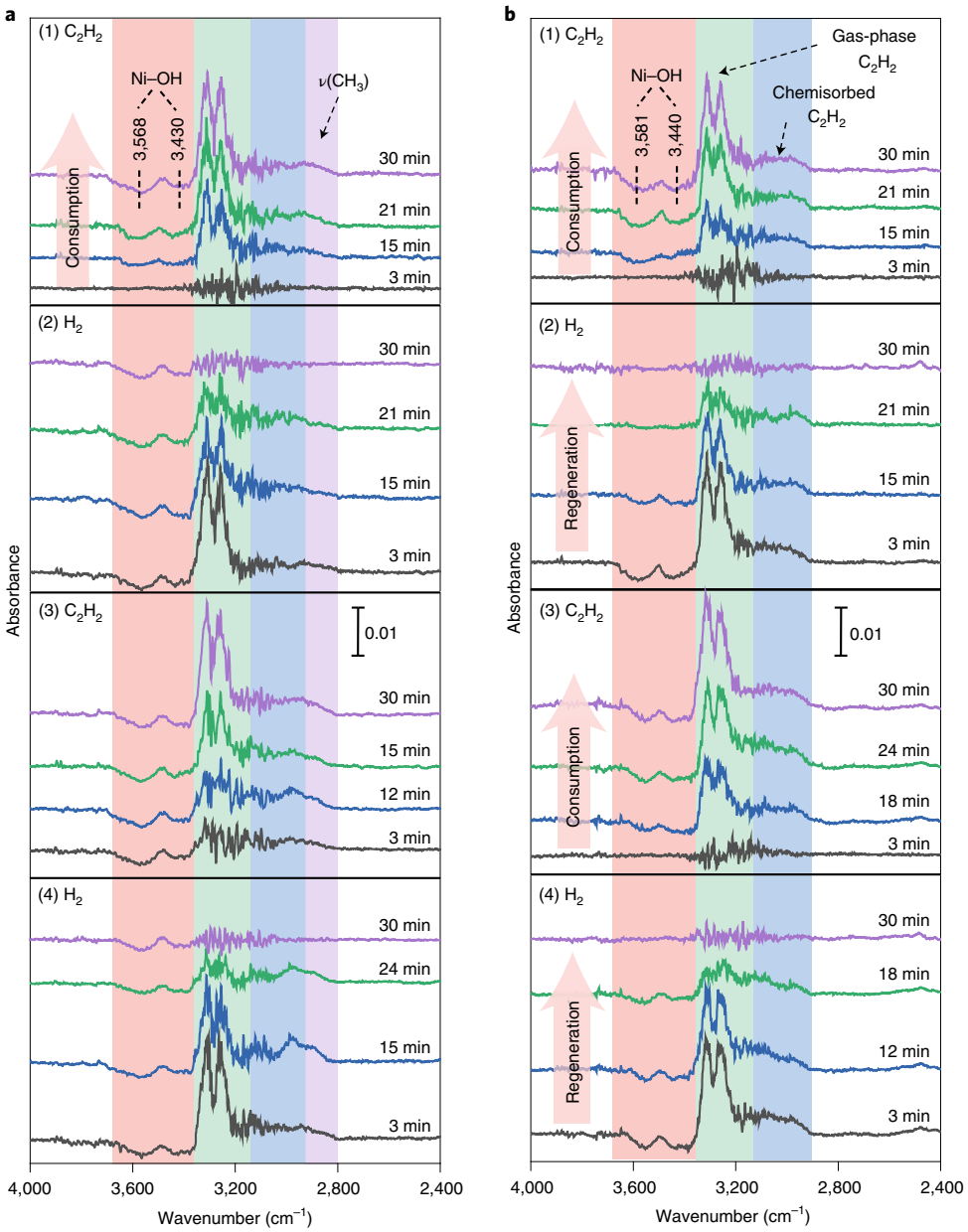

Fig. 3 | In situ DRIFTS investigation of C_2H_2 hydrogenation. a,**b**, In situ DRIFT spectra over $Ni_1/g\text{-}C_3N_4$ (**a**) and $Ni_1Cu_2/g\text{-}C_3N_4$ (**b**) catalysts after alternatively exposing to C_2H_2 and H_2 for different times with two consecutive C_2H_2 and H_2 cycles. The shaded regions with different colours highlight the variations in the peak position and intensity. Conditions: 0.03 g catalyst; 160 °C; 0.5% C_2H_2 or 5% H_2 in Ar; total flow, 6 ml min^{-1}.

used $Ni_1Cu_2/g\text{-}C_3N_4$ catalyst showed an identical result with the fresh sample (Supplementary Fig. 39), validating the excellent stability.

Theoretical insights into Ni_1 and Ni_1Cu_2 catalysts. Based on the above structural characterization and extensive DFT calculations, the Ni–Cu complex is identified as a chain-like Cu–OH–Ni–OH–Cu structure (Fig. 4a), whereas the Ni species in $Ni_1/g\text{-}C_3N_4$ after reduction forms the $Ni_1(OH)_2$ complex (Supplementary Fig. 40 and Supplementary Table 9). For the former one, the Ni atom bonds to N_{py} and C of $g\text{-}C_3N_4$ underneath, and is confined by Cu atoms from two sides via the bridging OH group; the Cu atoms are

Fig. 4 | Theoretical insights into stability and hydrogenation mechanism. a, Top view (left), side view (middle) and charge density difference (right) of the DFT-optimized structures of $Ni_1Cu_2/g\text{-}C_3N_4$ after reduction, where the Cu–Ni distances are highlighted. The orange, cyan, red and white balls denote copper, nickel, oxygen and hydrogen atoms, respectively. **b**, Stability of $Ni_1/g\text{-}C_3N_4$ and $Ni_1Cu_2/g\text{-}C_3N_4$ on C_2H_2 adsorption. The insets show the side view of the structures of the intermediates. **c**, Schematic of C–C-bond cleavage, and the Gibbs free energy (ΔG) of adsorption for acetylene or ethylene molecule on $Ni_1Cu_2/g\text{-}C_3N_4$ with pre-adsorbed acetylene at different temperatures at a total pressure of 0.1 MPa, 0.5% C_2H_2 and 25% C_2H_4. **d**, Optimized potential energy surfaces of acetylene hydrogenation reaction over $Ni_1Cu_2/g\text{-}C_3N_4$ with energy reference of acetylene and hydrogen molecule in the gas phase. The dashed line represents ethylene in the gas phase. Insets show the side view of the intermediate structures.

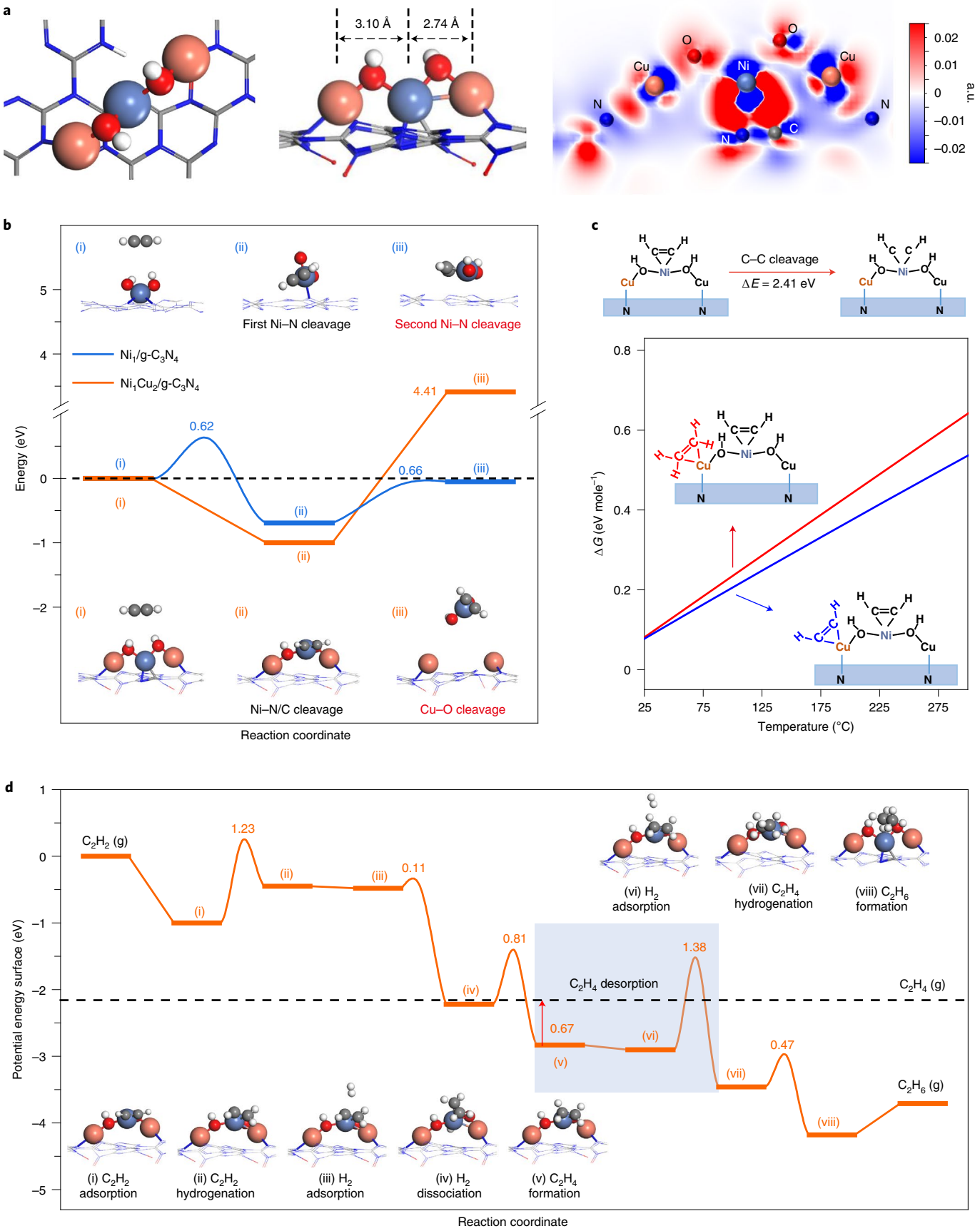
a
3.10 Å
2.74 Å
Cu
O
Ni
N
C
0.02
0.01
0
−0.01
−0.02
a.u.
b
(i)
(ii)
(iii)
First Ni–N cleavage
Second Ni–N cleavage
Ni1/g-C3N4
Ni1Cu2/g-C3N4
Energy (eV)
0.62
4.41
0.66
Ni–N/C cleavage
Cu–O cleavage
Reaction coordinate
c
C–C cleavage
ΔE = 2.41 eV
ΔG (eV mole−1)
Temperature (°C)
d
C2H2 (g)
1.23
0.11
0.81
1.38
0.67
0.47
C2H4 (g)
C2H6 (g)
C2H4 desorption
(i) C2H2 adsorption
(ii) C2H2 hydrogenation
(iii) H2 adsorption
(iv) H2 dissociation
(v) C2H4 formation
(vi) H2 adsorption
(vii) C2H4 hydrogenation
(viii) C2H6 formation
Potential energy surface (eV)
Reaction coordinate

further fastened on g-C_3N_4 via a strong Cu–N_{py} bond. Optimized bond lengths of Ni–O/N/C bond and Cu–O/N bond are in excellent agreement with the EXAFS data (Supplementary Table 10). The overall length of the optimized complex (5.84 Å) and two unequal Ni–Cu distances (2.74 and 3.10 Å) also perfectly agree with the STEM data (Supplementary Fig. 25). There is substantial charge accumulation between the Ni–C/N bonds and between the Cu–C/N bonds, while considerable charge transferring from Ni/Cu to high-lying OH groups (Fig. 4a and Supplementary Fig. 41); therefore, the characteristic covalent bond and ionic bond coexist between $Ni_1Cu_2(OH)_2$ and the g-C_3N_4 support, as well as in $Ni_1(OH)_2$/g-C_3N_4. Impressively, the formation of Ni_1Cu_2 linear trimer is energetically favourable, exothermic by 0.79 eV (Supplementary Fig. 42), manifesting the driving force for the linear trimer formation (Supplementary Fig. 6).

Different chemical stability of Ni_1/g-C_3N_4 and Ni_1Cu_2/g-C_3N_4 stems from the distinct structure change induced by stronger C_2H_2 adsorption, as found by DFT calculations and TPD measurements (Supplementary Fig. 30 and Supplementary Table 11). We found that acetylene adsorption on Ni_1/g-C_3N_4 has a modest barrier of 0.62 eV and exothermic by 0.69 eV (Fig. 4b), while simultaneously breaking one Ni–N/C support bond. The one Ni–N/C support bond left can be further broken only with a barrier of 0.66 eV. In other words, the Ni(OH)$_2$–C_2H_2 complex is rather mobile on g-C_3N_4, which would facilitate its aggregation to form Ni NPs, as found by STEM and XPS measurements (Supplementary Figs. 20 and 37). Obviously, strong Ni–support interaction alone is not sufficient to stabilize the Ni(OH)$_2$ complexes, although the bonding by the two Ni–N bonds (−2.93 eV) is considerably strong.

Acetylene adsorption on Ni_1Cu_2/g-C_3N_4 is stronger with an exothermic energy of 1.00 eV, in line with the TPD measurement (Supplementary Fig. 30). The optimized structure indicates that although acetylene adsorption breaks two interfacial Ni–N/C support bonds with practically no barrier, spatial confinement by two atomic Cu grippers from both sides through two bridging hydroxyls endows the breakages of the Cu–O support bond extremely endothermic by more than 4 eV, ensuring the high chemical stability of this catalyst during acetylene hydrogenation. Meanwhile, the two new Ni–C bonds formed with adsorbed C_2H_2 retain the overall CN of the Ni atom before and after acetylene adsorption (Fig. 4b and Supplementary Video 1), which is in good agreement with the X-ray absorption fine-structure (XAFS) data (Fig. 2g and Supplementary Table 10). Therefore, the resulting dynamics of Ni atoms via synergizing MSIs and spatial confinements ensures not only a facile structural transformation by breaking the Ni–N/C bonds to enhance acetylene adsorption but also a high chemical/thermal stability of SADCs free from aggregations (Supplementary Fig. 43).

Atomically dispersed and stable Ni atoms are beneficial to suppress C–C bond breaking and creating the prerequisite for the formation of graphitic coke and green oils due to the limited sites available (Fig. 4c and Supplementary Table 12). For instance, the cleavage of adsorbed acetylene is highly endothermic because of the absence of sites accommodating the broken CH* fragments. Moreover, after the preferential adsorption of acetylene at the Ni atom, the additional adsorption of acetylene or ethylene is only possible at the Cu sites with a weak binding energy of −0.55 and −0.51 eV, respectively, but will desorb at temperatures above room temperature. As a result, the formation of graphitic coke and green oils is prohibited on Ni_1Cu_2/g-C_3N_4, which is in excellent agreement with the in situ SVUV-PIMS and TGA measurements (Fig. 1e–g).

Optimized potential energy surface for the hydrogenation of acetylene over the $Ni_1(OH)_2Cu_2$ complex is shown in Fig. 4d and Supplementary Figs. 44–46. Acetylene is expected to be dominant on the Ni sites during hydrogenation, owing to its much stronger adsorption (−1.00 eV) than H_2 (−0.07 eV) (Supplementary Table 11). After acetylene adsorption, the proton in one bridging OH tends to directly attack the adsorbed acetylene with a barrier of 1.23 eV to form C_2H_3* (here * denotes surface species; Fig. 4d(i),(ii)). Next, hydrogen adsorbs on the Ni sites and effortlessly dissociates with one H atom in addition to C_2H_3* to form C_2H_4*, and the other one bonds to the Ni site (Fig. 4d(iii),(iv)). After that, the C_2H_4* species rearranges and the H atom transfers to the bridging O from Ni to regenerate the bridging OH with a low barrier of 0.81 eV. Compared with the sequential high hydrogenation barrier of 1.38 eV from ethylene to ethane, weakly bonded ethylene with a value of −0.67 eV boosts the desorption rate of ethylene—a key step for the high selectivity of Ni_1Cu_2/g-C_3N_4, which is in line with the catalytic results shown in Fig. 1. Obviously, the participation of bridging hydroxyls in the hydrogenation reaction suggested by DFT is in good agreement with the DRIFTS results (Fig. 3).

Conclusions

In summary, we have reported that synergizing MSIs and spatial confinement through Cu atomic grippers boosts the dynamics of highly loaded atomic Ni for efficient hydrogenations. Such dynamic and synergetic effects enable not only exceptionally high stability against both sintering and coke formation in the hydrogenation of acetylene but also lead the active sites to become highly adaptable towards both reactant adsorption and product desorption, thus boosting the activity (11 times higher than the conventional Ni_1/g-C_3N_4 catalyst) and ethylene selectivity. Compared with the literature[34–36], the synthesis of metal trimer catalysts using an atom-by-atom fabrication approach provides an avenue for the rational design of highly active and stable SADCs for practical application in selective chemical reactions.

Online content

Any methods, additional references, Nature Research reporting summaries, source data, extended data, supplementary information, acknowledgements, peer review information; details of author contributions and competing interests; and statements of data and code availability are available at https://doi.org/10.1038/s41565-021-00951-y.

Received: 11 December 2020; Accepted: 29 June 2021;
Published online: 26 July 2021

References

1. Wang, A. Q., Li, J. & Zhang, T. Heterogeneous single-atom catalysis. *Nat. Rev. Chem.* **2**, 65–81 (2018).
2. Liu, L. & Corma, A. Metal catalysts for heterogeneous catalysis: from single atoms to nanoclusters and nanoparticles. *Chem. Rev.* **118**, 4981–5079 (2018).
3. Marcinkowski, M. D. et al. Pt/Cu single-atom alloys as coke-resistant catalysts for efficient C–H activation. *Nat. Chem.* **10**, 325–332 (2018).
4. Akri, M. et al. Atomically dispersed nickel as coke-resistant active sites for methane dry reforming. *Nat. Commun.* **10**, 5181 (2019).
5. Kaiser, S. K. et al. Nanostructuring unlocks high performance of platinum single-atom catalysts for stable vinyl chloride production. *Nat. Catal.* **3**, 376–385 (2020).
6. Barbier, J. Deactivation of reforming catalysts by coking—a review. *Appl. Catal.* **23**, 225–243 (1986).
7. Gates, B. C., Flytzani-Stephanopoulos, M., Dixon, D. A. & Katz, A. Atomically dispersed supported metal catalysts: perspectives and suggestions for future research. *Catal. Sci. Technol.* **7**, 4259–4275 (2017).
8. Yang, X. F. et al. Single-atom catalysts: a new frontier in heterogeneous catalysis. *Acc. Chem. Res.* **46**, 1740–1748 (2013).
9. Huang, F. et al. Anchoring Cu_1 species over nanodiamond-graphene for semi-hydrogenation of acetylene. *Nat. Commun.* **10**, 4431 (2019).
10. Studt, F. et al. Identification of non-precious metal alloy catalysts for selective hydrogenation of acetylene. *Science* **320**, 1320–1322 (2008).
11. Huang, X. et al. Enhancing both selectivity and coking-resistance of a single-atom Pd_1/C_3N_4 catalyst for acetylene hydrogenation. *Nano Res.* **10**, 1302–1312 (2017).
12. Han, B. et al. Strong metal–support interactions between Pt single atoms and TiO_2. *Angew. Chem. Int. Ed.* **59**, 11824–11829 (2020).
13. Lang, R. et al. Single-atom catalysts based on the metal–oxide interaction. *Chem. Rev.* **120**, 11986–12043 (2020).

14. Liu, L. & Corma, A. Confining isolated atoms and clusters in crystalline porous materials for catalysis. *Nat. Rev. Mater.* **6**, 244–263 (2021).
15. Fu, Q. et al. Interface-confined ferrous centers for catalytic oxidation. *Science* **328**, 1141–1144 (2010).
16. Jones, J. et al. Thermally stable single-atom platinum-on-ceria catalysts via atom trapping. *Science* **353**, 150–154 (2016).
17. Wei, S. et al. Direct observation of noble metal nanoparticles transforming to thermally stable single atoms. *Nat. Nanotechnol.* **13**, 856–861 (2018).
18. Mitchell, S., Qin, R., Zheng, N. & Perez-Ramirez, J. Nanoscale engineering of catalytic materials for sustainable technologies. *Nat. Nanotechnol.*, **16**, 129–139 (2021).
19. Zhang, L., Zhou, M., Wang, A. & Zhang, T. Selective hydrogenation over supported metal catalysts: from nanoparticles to single atoms. *Chem. Rev.* **120**, 683–733 (2020).
20. Li, Z. et al. Well-defined materials for heterogeneous catalysis: from nanoparticles to isolated single-atom sites. *Chem. Rev.* **120**, 623–682 (2020).
21. Thomas, A. et al. Graphitic carbon nitride materials: variation of structure and morphology and their use as metal-free catalysts. *J. Mater. Chem.* **18**, 4893–4908 (2008).
22. Gao, G. P., Jiao, Y., Waclawik, E. R. & Du, A. J. Single atom (Pd/Pt) supported on graphitic carbon nitride as an efficient photocatalyst for visible-light reduction of carbon dioxide. *J. Am. Chem. Soc.* **138**, 6292–6297 (2016).
23. Lu, J. L., Elam, J. W. & Stair, P. C. Atomic layer deposition—sequential self-limiting surface reactions for advanced catalyst 'bottom-up' synthesis. *Surf. Sci. Rep.* **71**, 410–472 (2016).
24. George, S. M. Atomic layer deposition: an overview. *Chem. Rev.* **110**, 111–131 (2010).
25. Gould, T. D. et al. Synthesis of supported Ni catalysts by atomic layer deposition. *J. Catal.* **303**, 9–15 (2013).
26. Huo, J. S., Solanki, R. & McAndrew, J. Characteristics of copper films produced via atomic layer deposition. *J. Mater. Res.* **17**, 2394–2398 (2002).
27. Selander, N. & Szabo, K. J. Catalysis by palladium pincer complexes. *Chem. Rev.* **111**, 2048–2076 (2011).
28. Borodziński, A. & Bond, G. C. Selective hydrogenation of ethyne in ethene-rich streams on palladium catalysts. Part 1. Effect of changes to the catalyst during reaction. *Catal. Rev.* **48**, 91–144 (2006).
29. Liu, L., Zhao, C. & Li, Y. Spontaneous dissociation of CO_2 to CO on defective surface of Cu(I)/TiO_{2-x} nanoparticles at room temperature. *J. Phys. Chem. C.* **116**, 7904–7912 (2012).
30. Huang, L., Peng, F. & Ohuchi, F. S. 'In situ' XPS study of band structures at Cu_2O/TiO_2 heterojunctions interface. *Surf. Sci.* **603**, 2825–2834 (2009).
31. Biesinger, M. C., Payne, B. P., Lau, L. W. M., Gerson, A. & Smart, R. S. C. X-ray photoelectron spectroscopic chemical state quantification of mixed nickel metal, oxide and hydroxide systems. *Surf. Interface Anal.* **41**, 324–332 (2009).
32. Cao, L. et al. Identification of single-atom active sites in carbon-based cobalt catalysts during electrocatalytic hydrogen evolution. *Nat. Catal.* **2**, 134–141 (2018).
33. Moon, J. et al. Discriminating the role of surface hydride and hydroxyl for acetylene semihydrogenation over ceria through in situ neutron and infrared spectroscopy. *ACS Catal.* **10**, 5278–5287 (2020).
34. Tian, S. et al. Carbon nitride supported Fe_2 cluster catalysts with superior performance for alkene epoxidation. *Nat. Commun.* **9**, 2353 (2018).
35. Lu, Z. et al. An isolated zinc–cobalt atomic pair for highly active and durable oxygen reduction. *Angew. Chem. Int. Ed.* **58**, 2622–2626 (2019).
36. Kwak, J. H. et al. Molecular active sites in heterogeneous Ir–La/C-catalyzed carbonylation of methanol to acetates. *J. Phys. Chem. Lett.* **5**, 566–572 (2014).
37. Chai, Y. et al. Acetylene-selective hydrogenation catalyzed by cationic nickel confined in zeolite. *J. Am. Chem. Soc.* **141**, 9920–9927 (2019).
38. Dai, X. et al. Single Ni sites distributed on N-doped carbon for selective hydrogenation of acetylene. *Chem. Commun.* **53**, 11568–11571 (2017).
39. Shi, X. X. et al. Copper catalysts in semihydrogenation of acetylene: from single atoms to nanoparticles. *ACS Catal.* **10**, 3495–3504 (2020).
40. Huang, F. et al. Atomically dispersed Pd on nanodiamond/graphene hybrid for selective hydrogenation of acetylene. *J. Am. Chem. Soc.* **140**, 13142–13146 (2018).
41. Feng, Q. et al. Mesoporous nitrogen-doped carbon-nanosphere-supported isolated single-atom Pd catalyst for highly efficient semihydrogenation of acetylene. *Adv. Mater.* **31**, e1901024 (2019).
42. Pei, G. X. et al. Ag alloyed Pd single-atom catalysts for efficient selective hydrogenation of acetylene to ethylene in excess ethylene. *ACS Catal.* **5**, 3717–3725 (2015).
43. Pei, G. X. et al. Promotional effect of Pd single atoms on Au nanoparticles supported on silica for the selective hydrogenation of acetylene in excess ethylene. *New J. Chem.* **38**, 2043–2051 (2014).
44. Cao, Y. et al. Adsorption site regulation to guide atomic design of Ni–Ga catalysts for acetylene semi-hydrogenation. *Angew. Chem. Int. Ed.* **59**, 11647–11652 (2020).
45. Liu, Y. et al. Intermetallic Ni_xM_y (M = Ga and Sn) nanocrystals: a non-precious metal catalyst for semi-hydrogenation of alkynes. *Adv. Mater.* **28**, 4747–4754 (2016).
46. Armbrüster, M. et al. $Al_{13}Fe_4$ as a low-cost alternative for palladium in heterogeneous hydrogenation. *Nat. Mater.* **11**, 690–693 (2012).
47. Zhou, H. R. et al. PdZn intermetallic nanostructure with Pd–Zn–Pd ensembles for highly active and chemoselective semi-hydrogenation of acetylene. *ACS Catal.* **6**, 1054–1061 (2016).
48. Armbrüster, M., Wowsnick, G., Friedrich, M., Heggen, M. & Cardoso-Gil, R. Synthesis and catalytic properties of nanoparticulate intermetallic Ga–Pd compounds. *J. Am. Chem. Soc.* **133**, 9112–9118 (2011).
49. Liu, Y. N. et al. Layered double hydroxide-derived Ni-Cu nanoalloy catalysts for semi-hydrogenation of alkynes: improvement of selectivity and anti-coking ability via alloying of Ni and Cu. *J. Catal.* **359**, 251–260 (2018).
50. Chen, Y. J. & Chen, J. X. Selective hydrogenation of acetylene on SiO_2 supported Ni-In bimetallic catalysts: promotional effect of In. *Appl. Surf. Sci.* **387**, 16–27 (2016).

Methods

Materials. Copper(II) hexafluoroacetylacetonate hydrate ($Cu(hfac)_2$), formalin (37% formaldehyde in an aqueous solution) and bis(cyclopentadienyl) nickel(II) ($NiCp_2$) were bought from Shanghai Aladdin Bio-Chem Technology. Urea (99%), Cu_2O (99.9%), $Ni(NO_3)_2{\cdot}6H_2O$ (99%), $NaBH_4$ (99%), CuO (99%), $CaCl_2$ (99%) and NiO (99%) were purchased from Sinopharm Chemical Reagent. Nickel(II) phthalocyanine (NiPc), copper(II) phthalocyanine (CuPc) and $Ni/SiO_2{-}Al_2O_3$ catalyst (Ni loading, 66 wt%) were bought from Alfa Aesar. Lindlar Pd catalyst ($Pd{-}PbO/CaCO_3$) was purchased from TCI (Shanghai) Development. All the chemicals were used as received without further purification.

Ultrahigh-purity N_2 (99.999%), O_2 (99.999%), H_2 (99.999%) and Ar (99.999%), as well as gas mixtures including 10% O_2 in Ar, 10% H_2 in Ar, 0.5% C_2H_2, 5% H_2, 25% C_2H_4 in Ar, 1.2% 1,3-butadiene and 12% H_2 in Ar, were provided by Nanjing Special Gases.

Synthesis of g-C_3N_4 support. Urea was placed in a crucible and heated to 600 °C for 4 h in static air at a ramp rate of 5 °C min^{-1}. The resulting yellow material was milled into fine powders in a mortar. Next, the yellow powder was placed in an open ceramic container and heated at 550 °C for another 4 h. A light-yellow powder of g-C_3N_4 support was finally obtained.

Synthesis of Cu_1/g-C_3N_4 catalysts. Cu ALD was carried out on a viscous-flow stainless steel tube reactor system (ACME (Beijing) Technology) at 300 °C using $Cu(hfac)_2$ and formaldehyde as the precursors. Ultrahigh-purity N_2 (99.999%) was used as a carrier gas at a flow rate of 60 ml min^{-1}. The $Cu(hfac)_2$ precursor container was heated to 65 °C to reach a sufficient vapour pressure. The inlet manifold was held at 100 °C to avoid precursor condensation. The timing sequence was 300, 300, 40 and 180 s for $Cu(hfac)_2$ exposure, N_2 purge, formaldehyde exposure and N_2 purge, respectively. One, two, and ten cycles of Cu ALD were performed on g-C_3N_4 to obtain Cu_1(5.1%)/g-C_3N_4, Cu_1(8.1%)/g-C_3N_4 and Cu_1(11.4%)/g-C_3N_4 catalysts, respectively. When the $Cu(hfac)_2$ exposure time was reduced to 25 and 150 s for one cycle of Cu ALD on g-C_3N_4, Cu loadings of 0.5% and 2.7% were obtained, which were denoted as Cu_1(0.5%)/g-C_3N_4 and Cu_1(2.7%)/g-C_3N_4, respectively.

Synthesis of Ni_1/g-C_3N_4 and Ni_1Cu_2/g-C_3N_4 catalysts. NiO_x ALD was carried out on the g-C_3N_4 support at 240 °C using $NiCp_2$ and ozone as the precursors. The $NiCp_2$ precursor container was heated to 90 °C to achieve a sufficient vapour pressure. The inlet manifold was held at 115 °C to avoid precursor condensation on the inner walls. The timing sequence was 1,260, 200, 1,260 and 200 s for $NiCp_2$ exposure, N_2 purge, O_3 exposure and N_2 purge, respectively. Different $NiCp_2$ exposure times (from 100 to 1,260 s) were used on g-C_3N_4 to obtain a series of Ni single-atom catalysts with different Ni loadings (denoted as $Ni_1(x\%)$/g-C_3N_4, where x is the Ni loading). NiO_x ALD was also carried on the Cu_1(8.1%)/g-C_3N_4 samples with different $NiCp_2$ exposure times (from 200 to 1,260 s). The resulting samples were denoted as $Ni_1(x\%)Cu_1$(8.1%)/g-C_3N_4 (the optimized sample, namely, Ni_1(3.1%)Cu_1(8.1%)/g-C_3N_4, was denoted as Ni_1Cu_2/g-C_3N_4).

Morphology and compositions. Aberration-corrected HAADF-STEM measurements were taken on a JEM-ARM200F instrument (University of Science and Technology of China) at 200 keV. Meanwhile, energy-dispersive X-ray elemental mapping was also collected on the same equipment. Transmission electron microscopy and STEM measurements were performed on a JEOL JEM-2100F instrument operated at 200 keV.

Atomic-resolution EELS analysis of Cu–Ni–Cu line structures was performed on a Nion HERMES-100 instrument equipped with a C3/C5 corrector, operated at 60 kV with a convergence angle of around 32 mrad and a collection angle of about 75 mrad (University of Chinese Academy of Sciences). High-angle annular dark-field Z-contrast images were also collected for the same area, using an annular detector with a range of 75–210 mrad. To map out the dispersion of Ni $L_{2,3}$ edge and Cu $L_{2,3}$ edge signals in the line structures, we performed the EELS mapping with a probe current of about 11 pA, sampling with a pixel size of about 0.03 nm and a dwell time of 150 ms per pixel. To further improve the signal-to-noise ratio in the EELS experimental data, principal component analysis—a commonly used mathematical method to de-noise multidimensional datasets—was applied to the experimental raw data using HyperSpy (ref. [51]). The EELS data were recalibrated based on standard Cu and Ni spectra.

The Ni and Cu loadings of the catalysts were analysed by an inductively coupled plasma atomic emission spectrometer. The XRD spectra were recorded on a SmartLab X-ray diffractometer with a 9 kW rotating anode.

In situ SVUV-PIMS measurements. To study the formation of green oils, in situ SVUV-PIMS measurements were conducted on the mass spectrometry end-station (BL04B) at the National Synchrotron Radiation Laboratory, Hefei, China[52]. In brief, 150 mg of Ni_1Cu_2/g-C_3N_4 or Ni_1/g-C_3N_4 catalyst was loaded in a fixed-bed flow reactor, which was connected to the SVUV-PIMS system[53]. The catalyst was first reduced in 10% H_2 in Ar at a flow rate of 50 ml min^{-1} at 350 °C for 2 h and then cooled to 160 °C for Ni_1Cu_2/g-C_3N_4 and 200 °C for Ni_1/g-C_3N_4. After the sample temperature stabilized, a reaction gas consisting of 0.5% C_2H_2, 5% H_2 and 25% C_2H_4 balanced with Ar at a flow rate of 50 ml min^{-1} was then introduced into the quartz-tube reactor at a total pressure of 2 torr. The volatile components at the reactor outlet were ionized by the synchrotron vacuum ultraviolet light, and the formed ions were analysed by a home-made time-of-flight mass spectrometer at a photon energy of 12 eV. After 2 h of continuous data collection, the reaction gas was switched to pure Ar; then, the the sample temperature was gradually increased at a heating rate of 5 °C min^{-1} to 300 °C, while the composition of accumulated green oils on the two samples was analysed by the online SVUV-PIMS spectrometer.

In situ TGA measurements. In situ TGA measurements were performed on a TGA550 instrument (TA Instruments) equipped with an evolved gas analysis furnace to quantify coke formation during the semi-hydrogenation of acetylene. After loading the sample into the furnace, the sample was heated to 350 °C at a heating rate of 3 °C min^{-1} in 10% H_2/Ar (25 ml min^{-1}) and then isothermally maintained for 2 h to reduce the sample. Next, the sample was cooled to a specified temperature in argon (25 ml min^{-1}) and isothermally maintained for 1 h to stabilize the instrument. Next, acetylene hydrogenation gas consisting of 0.5% acetylene, 5% H_2 and 25% ethylene balanced with Ar was introduced into the sample at a flow rate of 25 ml min^{-1} for about 12 h at the specified temperature. The change in sample weight with time during acetylene hydrogenation was recorded. Here the temperatures for acetylene hydrogenation were 160 and 200 °C for Ni_1Cu_2/g-C_3N_4 and Ni_1/g-C_3N_4 catalysts, respectively, to ensure a similar initial conversion for these samples.

In situ XPS measurements. In situ XPS and Auger spectra measurements were conducted at the BL10B beamline photoemission end-station at the National Synchrotron Radiation Laboratory, Hefei, China. In brief, the beamline is connected to a bending magnet and covers photon energies from 100 to 1,000 eV. The end-station consists of four chambers, namely, analysis chamber, preparation chamber, quick sample load-lock chamber and high-pressure reactor. The analysis chamber, with a base pressure of $<5\times10^{-10}$ torr, is connected to the beamline and equipped with a VG Scienta R3000 electron energy analyser and a twin-anode X-ray source. The high-pressure reactor houses a reaction cell where the samples can be treated with different gases up to 20 bar and simultaneously heated up to 650 °C. After sample treatment, the reactor can be pumped down to a high vacuum ($<10^{-8}$ torr) for sample transfer.

In this work, after loading the as-prepared Ni_1Cu_2/g-C_3N_4 sample into the chamber, a set of XPS spectra in the Ni2*p*, Cu2*p*, N1*s*, C1*s* and O1*s* regions were first recorded without any treatment (denoted as Ni_1Cu_2/g-C_3N_4). Next, the sample was transferred back into the high-pressure reactor and reduced in 10% H_2 in Ar at 350 °C for 2 h at atmosphere pressure. Another set of XPS spectra were collected after transferring back to the analysis chamber. The reduced sample was denoted as Ni_1Cu_2/g-C_3N_4-R. Finally, the sample was exposed to the acetylene hydrogenation stream consisting of 0.5% C_2H_2, 5% H_2 and 25% C_2H_4 balanced with Ar in the high-pressure reactor at 160 °C for another 1 h. Another set of XPS spectra were then collected after the hydrogenation-reaction gas treatment without exposing to air, which was denoted as Ni_1Cu_2/g-C_3N_4-H. Similarly, XPS spectra of the Ni_1/g-C_3N_4 sample were also collected following the same procedure. The XPS spectra of the sample after reduction at 350 °C for 2 h and exposing the reaction gas at 200 °C for another 1 h were denoted as Ni_1/g-C_3N_4-R and Ni_1/g-C_3N_4-H, respectively. The C1*s* binding energy at 284.8 eV was used as an internal reference.

In situ XAFS. In situ XAFS measurements at the Ni K edge (8,333 eV) and Cu K edge (8,979 eV) were performed in the transmission mode with the Si(311) monochromator at the BL14W1 beamline at the Shanghai Synchrotron Radiation Facility (SSRF), China. The storage ring at the SSRF worked at 3.5 GeV with a maximum current of 210 mA (ref. [54]). A home-made reaction cell was used for the operando experiments, which allows exposing the sample to different pretreatment gases or reactions gases, as well as sample heating up to 400 °C.

Typically, the as-prepared Ni_1Cu_2/g-C_3N_4 sample was put into the reaction cell and purged with He for 10 min at room temperature; then, the XAFS spectra were recorded at both Ni and Cu K edges (denoted as Ni_1Cu_2/g-C_3N_4). After that, the sample was reduced in 10% H_2 in He at 350 °C for 2 h. After cooling the sample to 160 °C in 10% H_2 in He, the XAFS spectrum was recorded at the Ni K edge and Cu K edge, which was denoted as Ni_1Cu_2/g-C_3N_4-R. Finally, the sample was exposed to the acetylene hydrogenation reaction stream consisting of 0.5% C_2H_2, 5% H_2 and 25% C_2H_4 balanced with Ar at 160 °C for another 1 h, and the XAFS spectra were sequentially recorded at the Ni and Cu K edges, which were denoted as Ni_1Cu_2/g-C_3N_4-H. Similarly, in situ XAFS measurements of Ni_1/g-C_3N_4 were also collected following the same procedure but only collecting the XAFS spectra at the Ni K edge. The XAFS spectra of the sample after reduction at 350 °C for 2 h were denoted as Ni_1/g-C_3N_4-R.

The acquired EXAFS data were processed according to standard procedures using the ARTEMIS module implemented in the IFEFFIT software package. The EXAFS oscillation functions $\chi(k)$ were obtained by subtracting the post-edge background from the overall absorption spectra and then normalized with respect to the edge-jump step.

In terms of the Ni K edge, fittings were done in the interatomic distance (R) space within the R range of 0.8–3.0 Å^{-1} for k^3-weighted $\chi(k)$ functions with Hanning windows ($dk = 1.0$ Å^{-1}) and a k range of 2.3–10.4 Å^{-1} was used; during curve fittings, the amplitude reduction factor S_0^2 was fixed at a value of 0.78 determined by fitting the data of Ni foil. For fitting the EXAFS data of the Ni_1Cu_2/g-C_3N_4 sample, the energy shift (ΔE_0) values for the Ni–C/N bonds were fixed to reduce the number of adjustable parameters and to break the strong correlation between ΔE_0 and R. In terms of the Cu K edge, the R range of 1.0–3.0 Å^{-1} and k range of 2.9–12.4 Å^{-1} were used; during curve fittings, the amplitude reduction factor S_0^2 was fixed at 0.9 as determined by fitting the data of Cu foil. Debye–Waller factor (σ^2), N, R and ΔE_0 were treated as adjustable parameters during the fitting process.

The yielded R factors of all the samples are not larger than 0.008, indicating good fitting qualities.

TPD measurements. The C_2H_2 and C_2H_4 TPD experiments were performed on a Micromeritics AutoChem II chemisorption analyser, which was connected to a Pfeiffer OmniStar mass spectrometer. In a typical experiment, 50 mg sample was first reduced in 10% H_2/He at 350 °C for 2 h and then purged with He at 300 °C for 1 h. Next, the sample was cooled down to room temperature in He; then, C_2H_2 or C_2H_4 gas was introduced into the sample until saturation. Subsequently, the sample was purged with He at 25 °C for 1 h and then the sample temperature was gradually increased at a heating rate of 10 °C min^{-1} in He from 25 to 300 °C while recording the TPD data.

In situ DRIFTS. In situ DRIFTS was performed on a Thermo Nicolet iS10 FTIR spectrometer equipped with a mercury–cadmium–telluride detector at a resolution of 4 cm^{-1} and 128 scans. First, 30 mg of the sample was placed in a high-temperature cell (Harrick) with CaF_2 windows. For in situ DRIFTS of CO chemisorption, the sample was first reduced in 10% H_2 in Ar at 350 °C for 2 h. Then, the sample was cooled down to 25 °C in Ar. After that, the sample was exposed to 10% CO/Ar (30 ml min^{-1}) for 30 min until saturation and the spectra were continuously collected during this process. The CO chemisorption spectra were obtained by subtracting the CO chemisorption DRIFT spectrum of g-C_3N_4 to remove the gas-phase CO.

As for in situ DRIFTS of C_2H_2 or C_2H_4 hydrogenation, the sample was first reduced in 10% H_2 in Ar at 350 °C for 2 h. Then, the sample was cooled down to 160 °C in Ar and kept for 30 min while the spectra were collected. After that, the experiments were repeated by sequentially exposing to C_2H_2 and H_2 for C_2H_2 hydrogenation or sequentially exposing to C_2H_4 and H_2 for C_2H_4 hydrogenation. The total flow rate was 6 ml min^{-1}. It should be noted that all the gases were passed through a calcium chloride filter at −40 °C in the gas inlet line before the Harrick cell to remove trace water from the gas.

As for in situ DRIFTS of water adsorption, the sample was first reduced in 10% H_2 in Ar at 350 °C for 2 h. Then, the sample was cooled down to 25 °C in Ar. After that, the sample was exposed to 5% H_2O/Ar (6 ml min^{-1}) for 30 min until saturation, and the spectra were continuously collected during this process.

Catalytic activity test. Selective hydrogenation of acetylene in excess ethylene was conducted in a fixed-bed flow reactor. The total flow rate was kept at 30 ml min^{-1}. The amount of non-precious catalyst was 150 mg, which was diluted with 1 g of 200 mesh quartz chips. Before the reaction test, all the catalysts were reduced in 10% H_2 in Ar at 350 °C for 2 h. Then, the feed gas—consisting of 0.5% acetylene, 5% H_2 and 25% ethylene with Ar as the balance gas—was introduced into the reactor to start the reaction. Next, acetylene conversion of all these catalysts was increased by increasing the reaction temperature. The reaction products were analysed using an online gas chromatograph (A91, Panna Instrument) equipped with a flame ionization detector and a capillary column (ValcoPLOT VP–alumina–KCl; 50 m × 0.53 mm). The acetylene conversion and ethylene selectivity were calculated using the following equations, respectively:

$$C_2H_2\ \text{conversion}\ (\%) = \left(\frac{[C_2H_2]_{in} - [C_2H_2]_{out}}{[C_2H_2]_{in}}\right) \times 100 \quad (1)$$

$$C_2H_4\ \text{selectivity}\ (\%) = \left(1 - \frac{[C_2H_6]_{out} + 2\,[C_4]_{out}}{[C_2H_2]_{in} - [C_2H_2]_{out}}\right) \times 100 \quad (2)$$

$[C_2H_2]_{in}$ and $[C_2H_2]_{out}$ are the concentrations of acetylene at the inlet and outlet of the reactor, respectively. $[C_2H_6]_{out}$ and $[C_4]_{out}$ are the concentrations of ethane and total C_4 products at the outlet of the reactor, respectively.

For the kinetic measurements, we reduced the amount of catalyst and increased the flow rate of the reaction gas to ensure that the acetylene conversion was below 15%. Turnover frequencies (TOFs) of the non-precious catalysts were calculated using the following equation:

$$\text{TOFs} = \frac{\text{Mole of } C_2H_2 \text{ converted per hour}}{D \times n_{metal}} \quad (3)$$

Here n_{metal} is the mole of Ni or Cu. For Ni_1Cu_2/g-C_3N_4, n_{metal} is the mole of Ni. Also, D is the dispersion of metal NPs or clusters/atoms; $D = 1$ for Ni_1/g-C_3N_4, Cu_1/g-C_3N_4 and Ni_1Cu_2/g-C_3N_4.

Semi-hydrogenation of 1,3-butadiene was also recorded on the same reaction test station and using the same gas chromatograph. The feed gas consists of 1.2% 1,3-butadiene, 12% H_2 with Ar as the balance gas. The same pretreatment was performed on all the catalysts before the reaction test. Here 1,3-butadiene conversion and butene selectivity were calculated using the following equations, respectively:

$$1,3\text{-butadiene conversion}\ (\%) = \left(\frac{[1,3\text{-butadiene}]_{in} - [1,3\text{-butadiene}]_{out}}{[1,3\text{-butadiene}]_{in}}\right) \times 100 \quad (4)$$

$$\text{Butene selectivity}\ (\%) = \left(\frac{[\text{Butene}]_{out}}{[\text{Butene}]_{out} + [\text{Butane}]_{out}}\right) \times 100 \quad (5)$$

$[1,3\text{-butadiene}]_{in}$ and $[1,3\text{-butadiene}]_{out}$ are the concentrations of 1,3-butadiene at the inlet and outlet of the reactor, respectively. $[\text{Butene}]_{out}$ and $[\text{Butane}]_{out}$ are the concentrations of butene and butane at the outlet of the reactor, respectively.

Computational methods and models. All the spin-polarized calculations were performed using DFT calculations implemented in the Vienna ab initio simulation package[55]. We described the electron–ion interaction using the projector augmented wave method[56]. The exchange–correlation interaction was described by the optB86b-vdW functional (ref. [57]). The Kohn–Sham equations were solved by using a plane-wave basis set with a kinetic energy cutoff of 400 eV. The convergence criterion for electronic self-consistent interactions is 10^{-4} eV. The geometries of bulk and surface were optimized by the conjugate gradient algorithm until the maximum force on any ion was less than 0.02 eV Å^{-1}. All the transition states were determined by using the climbing image nudged elastic band method[58] with confirmation of vibrational analysis. The transition states are optimized until all the forces are below 0.05 eV Å^{-1}.

The g-C_3N_4 was modelled by a (2 × 2) supercell of a single-layer g-C_3N_4, where all the atoms in the supercell were fully relaxed. A (3 × 3 × 1) Monkhorst–Pack k-point mesh was used to sample the surface Brillouin zone. A 20 Å vacuum was introduced to avoid interaction from adjacent cells. The reaction energy and barrier are calculated as $\Delta E = E_{FS} - E_{IS}$ and $E_a = E_{TS} - E_{IS}$, where E_{IS}, E_{FS} and E_{TS} are the energies of the corresponding initial state, final state and transition state, respectively.

Data availability

Source data are provided with this paper. The data that support the findings of this study are available from the corresponding authors upon reasonable request.

References

51. de la Peña, F. et al. hyperspy/hyperspy: HyperSpy v.1.5.2 (Zenodo, 2019).
52. Zhou, Z. et al. The vacuum ultraviolet beamline/endstations at NSRL dedicated to combustion research. *J. Synchrotron Rad.* **23**, 1035–1045 (2016).
53. Luo, L. F. et al. Gas-phase reaction network of Li/MgO-catalyzed oxidative coupling of methane and oxidative dehydrogenation of ethane. *ACS Catal.* **9**, 2514–2520 (2019).
54. Yang, H. B. et al. Atomically dispersed Ni(I) as the active site for electrochemical CO_2 reduction. *Nat. Energy* **3**, 140–147 (2018).
55. Kresse, G. & Furthmuller, J. Efficiency of ab-initio total energy calculations for metals and semiconductors using a plane-wave basis set. *Comput. Mater. Sci.* **6**, 15–50 (1996).
56. Kresse, G. & Joubert, D. From ultrasoft pseudopotentials to the projector augmented-wave method. *Phys. Rev. B* **59**, 1758–1775 (1999).
57. Klimeš, J., Bowler, D. R. & Michaelides, A. Van der Waals density functionals applied to solids. *Phys. Rev. B* **83**, 195131 (2011).
58. Henkelman, G., Uberuaga, B. P. & Jonsson, H. A climbing image nudged elastic band method for finding saddle points and minimum energy paths. *J. Chem. Phys.* **113**, 9901–9904 (2000).

Acknowledgements

This work was supported by the National Key R&D Program of China (2018YFA0208603 and 2017YFA0402800); the National Natural Science Foundation of China (22025205, 21673215, 91645202, 91845203, 11621063 and 91945302); the Frontier Science Key Project of the Chinese Academy of Sciences (CAS) (QYZDJ-SSW-SLH054); the Dalian National Laboratory for Clean Energy (DNL) Cooperation Fund (DNL201907 and DNL201920); Beijing Outstanding Young Scientist Program (BJJWZYJH01201914430039); Key Research Program of Frontier Sciences, CAS (QYZDB-SSW-JSC019); Bureau of Frontier of Sciences and Education, CAS (ZDBS-LY-SLH003); the Fundamental Research Funds for the Central Universities (WK2060030029 and WK3430000005); Users with Excellence Program of Hefei Science

Center, CAS (2019HSC-UE016); and the Max Planck Partner Group. We also gratefully thank the BL14W1 beamline at the Shanghai Synchrotron Radiation Facility (SSRF), and the BL10B and BL04B beamlines at the National Synchrotron Radiation Laboratory (NSRL), China, and the Supercomputing Center, University of Science and Technology of China.

Author contributions

J.L. designed the experiments and W.-X.L. designed the DFT calculations. J.G. performed the catalytic performance evaluation. S.W., L.H., Z.S., L.C. and S.C. performed the XAFS measurements. M.J. performed the DFT calculations. Y.P., J.Y. and W.W. performed the SVUV-PIMS measurements. Y.L. conducted the HAADF-STEM measurements. A.L. and W.Z. performed the atomic-resolution EELS measurements. H.-J.W., X.L. and L.W. performed the TEM measurements. X.S. and X.H. performed the TGA measurements. X.Z., H.P. and J.Z. performed the XPS measurements. J.L. and W.-X.L. co-wrote the manuscript, and all the authors contributed to the overall scientific interpretation and edited the manuscript. We gratefully thank P. C. Stair for his insightful suggestions and manuscript polishing.

Competing interests

The authors declare no competing interests.

Additional information

Supplementary information The online version contains supplementary material available at https://doi.org/10.1038/s41565-021-00951-y.

Correspondence and requests for materials should be addressed to S.W., W.-X.L. or J.L.

Peer review information *Nature Nanotechnology* thanks Dehui Deng and the other, anonymous, reviewer(s) for their contribution to the peer review of this work.

Reprints and permissions information is available at www.nature.com/reprints.